Transactions of Materials Research 1 (2025) 100016

Contents lists available at ScienceDirect

Transactions of Materials Research

journal homepage: www.sciencedirect.com/journal/transactions-of-materials-research

Grain boundary segregation mediated highly stable and high performance nanostructured MgAgSb bulk thermoelectric materials

Lei Jiao [a], Liangjun Xie [b], Yu-Ke Zhu [a,b], Lankun Wang [a], Yuxin Sun [b], Yuan Yu [c], Alexandra Ivanova [d], Vladimir Khovaylo [d], Fengkai Guo [b], Wei Cai [b], Jiehe Sui [b], Zihang Liu [a,*]

[a] *State Key Laboratory of Precision Welding & Joining of Materials and Structures, Harbin Institute of Technology, Harbin, 150001, China*
[b] *National Key Laboratory for Precision Hot Processing of Metals, Harbin Institute of Technology, Harbin, 150001, China*
[c] *Institute of Physics (IA), RWTH Aachen University, Sommerfeldstraße 14, Aachen, 52074, Germany*
[d] *National University of Science and Technology (NUST MISIS), Moscow, 119049, Russia*

ARTICLE INFO

Keywords:
Thermal stability
Nanostructure
Thermoelectric
Grain boundary
MgAgSb

ABSTRACT

We systematically elaborate the thermal stability mechanism of MgAgSb-based materials through thermodynamic and kinetic analysis of grain boundary characterizations. By proposing the general strategy of grain boundary segregation engineering (GBSE) to improve the stability of nanostructured bulk thermoelectric materials, it is found that excessive Cu doping can modify the microstructure to enhance stability as both Ag and Cu segregation coexist at the grain boundary. After annealing at elevated temperature, the final performance is almost unchanged with a high room-temperature dimensionless figure-of-merit zT of around 0.7, in contrast to property deterioration of pure MgAgSb. As revealed by atom probe tomography (APT) measurements, Cu segregation inhibits grain boundary migration and hinders grain growth, due to the additional reduced grain boundary energy and mobility. Our work provides new insights into the critical role of grain boundary segregation in the properties optimization and thermal stability enhancement, which opens up alternative perspectives for designs of highly stable and high-performance nanostructured thermoelectric materials.

1. Introduction

With the increasing global energy crisis and environmental pollution, developments of clean and sustainable energy conversion technologies have received intensive attention. Waste heat accounts for about 60% of the total energy consumption and more than half is the low-grade waste heat with a temperature below 300°C, which lacks effective recycling technologies due to the low energy density and temperature difference [1]. Thermoelectric power generation enables the direct conversion of waste heat into electricity, which is considered to be one of the most promising approaches to harvesting energy with the unique advantages of no pollution, no moving parts, high reliability, and long service life [2,3]. The energy conversion efficiency (η) of the thermoelectric (TE) device is determined by the dimensionless figure of merit (zT), which is defined as $zT = S^2T/(\rho\kappa)$, where S, T, ρ, and κ are the Seebeck coefficient, absolute temperature, electrical resistivity, and thermal conductivity, respectively. S^2/ρ is called the power factor (PF), indicating the electrical properties. However, the thermal and electrical transport parameters are strongly interdependent and coupled, making the realization of high TE performance full of challenges [4–6].

Bi_2Te_3-based alloys are the major TE materials near room temperature [7], while the extremely rare constituent element tellurium and poor mechanical properties limit their large-scale applications [8]. In search for a better alternative, the p-type α-MgAgSb-based materials have attracted intensive interest in TE cooling and energy harvesting below 300°C [9], with abundant elements, excellent mechanical [10] and TE properties [11,12]. As reported by Kirkham et al. [13] in 2012, it was found that there are two other polymorphs besides α-phase MgAgSb, a Cu_2Sb-type β-phase and a cubic γ-phase at high temperatures. At the material level, the synthesis routes to obtain pure α-MgAgSb have been modified by different groups [14,15]. The origin of its Phonon Glass Electron Crystal (PGEC) behaviors and strategies to enhance TE properties have been extensively explored, such as optimizing carrier concentration to increase power factor [16,17], and intrinsic Ag vacancy engineering [18,19] to suppress lattice thermal conductivity κ_{lat}. At the device level, coupled with high-performance n-type $Mg_3(Bi, Sb)_2$, p-type α-MgAgSb-based alloys have participated in the fabrication of Te-free TE devices for near-room temperature cooling and power generation

---

* Corresponding author.
E-mail address: zihangliu@hit.edu.cn (Z. Liu).

https://doi.org/10.1016/j.tramat.2025.100016
Received 21 March 2025; Received in revised form 8 April 2025; Accepted 8 April 2025

[20–23].

Nanostructured materials exhibit many unique physical, chemical and mechanical properties that can break the limit of conventional materials with coarse grains [24]. The reduction in grain size creates high volume fraction of grain boundaries (GBs) and interfaces, which is accompanied by an increase in the total Gibbs free energy of the system, as a driving force for grain growth to lower the excess interfacial energy [25]. This in turn produces high susceptibility to structural failure for nanostructured metallic materials. Therefore, the thermal stability is critical in evaluating the service capability, which can be defined as the ability to resist an apparent grain coarsening at elevated temperatures [26]. For some typical examples in TE materials, Sb_2Te_3 alloys with nanograins and nanotwins constructed by high energy ball milling have suffered from high-temperature softening [27]. Phase-separated nanostructured p-type ternary lead chalcogenides require appropriate post processing to avoid significant precipitate growth and performance deterioration during thermal cycles [28].

Owing to stronger phonon scattering caused by multiple-scale microstructure defects, nanostructuring has been proven to be an effective approach to enhance zT value by reducing the κ_{lat} [29,30]. Xie et al. obtained ultralow κ_{lat} by constructing ultrafine grains within the nanocrystalline regime and randomly distributed pores [31], which makes the nanograined α-MgAgSb competitive for TE refrigeration applications. However, when applied to energy harvesting at high temperatures, nanograined α-MgAgSb could suffer from abnormal grain growth due to high-density GBs, and the correlation between GB features and TE properties should be concerned. Moreover, the low phase transition temperature may promote the formation of impurity phases and speed up the growth of grains, thus leading to significant damage in TE performance. In addition, small grains and nanoprecipitates may restrict the long-term thermal stability at elevated temperature.

Herein, our work investigates the property optimization and the thermal stability mechanism of nanostructured MgAgSb-based materials, which were systematically elaborated through detailed microstructural characterizations and TE properties measurements. It is found that annealing at 548 K for two days significantly worsens TE properties, compared to their excellent long-term thermal stability after annealing for 28 days at 523 K. Atom probe tomography (APT) measurements focus on the grain boundary characteristics to understand the correlation between microstructure and thermal stability. For nanostructured pure $MgAg_{0.97}Sb_{0.99}$, the segregation of Ag at GBs may reduce the GB energy and realize a solute drag effect, which can be helpful for thermodynamic and kinetic stabilization of the nanostructure. Based on the strategy of grain boundary segregation engineering, extra Cu segregation at GBs is achieved through excessive doping as revealed by APT. We suppose that Cu doping can further modify the GB complexions and enhance the thermal stability.

2. Experimental details

2.1. Synthesis

The powder with a stoichiometric composition of $MgAg_{0.97}Sb_{0.99}$ was prepared with a two-step high-energy ball milling approach. High-purity magnesium (Mg 99.99%, Aladdin) and silver (Ag, 99.999%, Aladdin) particles were weighed in the argon-filled glove box and loaded into a stainless-steel jar with stainless-steel ball. After 10 h of ball milling in the high energy ball mill (SPEX-8000M Mixer/Mill) at the speed of 1200 rpm/min, the antimony (Sb, 99.999%, Alfa Aesar) was added into the jar in the glove box with another ball milling of 10 h, the copper (Cu, 99.999%, Aladdin) for doping was also added at this step and the doping amount was 10%, the total weight of raw materials is about 8 g. The prepared powder was loaded into a graphite die with an inner diameter of 12.7 mm and sintered by hot press sintering (HP) at 573 K for 30 min in a vacuum under the pressure of 80 MPa. Before structure characterizations and property measurements, the as-sintered samples were annealed for 30 min at 573 K. The samples were placed in sealed vacuum quartz tubes and annealed in the muffle furnace for a long time.

2.2. Structure characterizations

The phase structure was analyzed by X-ray diffraction (XRD, PANalytical X'Pert Pro) using Cu K_α radiation. The microstructures of the samples were investigated with a scanning electron microscope (SEM, Quanta 200 FEG) and an electron probe microanalyzer (EPMA, JXA-8230). APT was used to analyze atomic-scale composition at/or near GBs. Site-specific specimens were prepared by the method of dual-beam scanning electron microscope/focused ion beam (SEM/FIB, Helios NanoLab650, FEI). APT measurements were performed on a local electrode atom probe instrument (LEAP™ 5000 XS, CAMECA) in laser mode with a pulse energy of 10 pJ and pulse repetition rate of 200 kHz at a base temperature of 40 K, and an ion flight path of 100 mm. The data reconstruction and analysis were processed using AP Suite 6.3.

2.3. Property measurements

The electrical conductivity σ and Seebeck coefficient S were measured using ZEM-3 (Ulvac-Riko, Inc. Japan). Thermal conductivity was calculated using $\kappa_{\mathrm{tot}} = D\rho C_{\mathrm{p}}$, where the density ρ was measured by the Archimedes method, the thermal diffusivity D was measured by a laser flash method (LFA 457, Netzsch), and the specific heat capacity C_{p} was measured with a differential scanning calorimetry (DSC-404F3, Netzsch). The measurement uncertainties for σ, S, κ_{tot} are ±3, ±5, and ±7%, so the combined uncertainties of PF and zT are ±13% and ±20%, respectively. The room temperature Hall coefficients (R_{H}) were measured based on the van-der-Pauw method under a reversible magnetic field of 1.5 T. The Hall carrier concentration n_{H} and Hall carrier mobility μ_{H} were calculated by using the relationships $n_{\mathrm{H}} = 1/(eR_{\mathrm{H}})$ and $\mu_{\mathrm{H}} = \sigma R_{\mathrm{H}}$, respectively.

3. Results and discussion

For previously reported low-temperature thermoelectric devices consisting of p-type α-MgAgSb, the hot-side temperatures corresponding to the maximum conversion efficiency were mostly tested between 523 K and 593 K. Therefore, in order to evaluate the thermal stability of nanostructured pure $MgAg_{0.97}Sb_{0.99}$, we selected the temperatures of 523 K and 548 K respectively, and carried out the vacuum-annealing process for two days.

Fig. 1a shows the XRD patterns of the annealed samples. After annealing at 523 K for two days, all the diffraction peaks are consistent with the as-sintered pure phase sample. However, a distinct impurity phase diffraction peak appears after annealing at 548 K corresponding to the peak of Ag_3Sb phase. In contrast to the backscattered electron (BSE) and the secondary electron (SE) images of the sample annealed at 523 K, vacuum annealing at 548 K results in abnormal grain growth to the micrometer scale and the formation of diffusely dispersed impurity phase (Fig. 1b). The wavelength dispersive spectrometer (WDS) point-scanning data (Table S1) detected from EPMA also confirm the phase composition close to Ag_3Sb.

The TE properties of the sample have deteriorated apparently after annealing for two days at 548 K while only slight changes would occur under 523 K. As reported by Ying et al. [15], the carrier concentration of the $MgAg_{0.97}Sb_{0.99}$ sample is 7.3×10^{19} cm^{-3} with a trace of Ag_3Sb and Sb impurity phases (2.1%), much higher than our as-sintered pure phase sample (2.7×10^{19} cm^{-3}). Therefore, it can be inferred that the decreases in electrical resistivity ρ and Seebeck coefficient S (Fig. 1c and d) are due to the formation of the Ag_3Sb impurity phase, which increase the carrier concentration significantly and inhibit the intrinsic excitation, and the abnormal growth of the grains reduces the scattering of carriers, leading to increase in mobility. The calculated PF above 400 K is lower than the as-sintered sample as intrinsic excitation moves to the higher

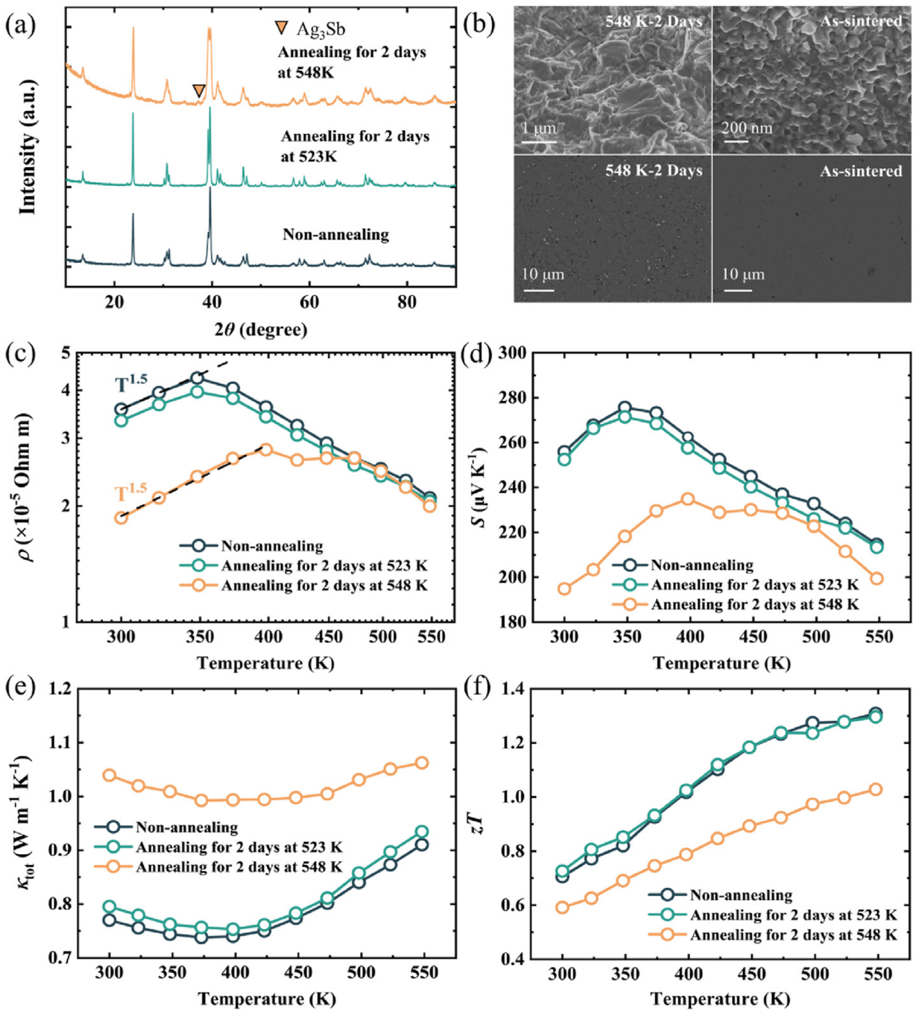

Fig. 1. Microstructure and TE properties of nanostructured $MgAg_{0.97}Sb_{0.99}$ annealed for two days at 548 K. (a) XRD patterns, (b) SEM images of the polished surface and the fracture morphology, compared with the results of as-sintered sample, (c) temperature-dependent electrical resistivity ρ, (d) Seebeck coefficient S, (e) total thermal conductivity κ_{tot}, (f) figure of merit zT.

temperature, as shown in Fig. S1a. Annealing at 548 K increases the total thermal conductivity κ_{tot} at 300 K from 0.77 W m^{-1} K^{-1} to 1.04 W m^{-1} K^{-1} (Fig. 1e), where both electronic thermal conductivity κ_{ele} and lattice thermal conductivity κ_{lat} sharply increase (Fig. S1b), owing to the distribution of the metal-like Ag_3Sb impurity phase. The κ_{ele} is defined by the relationship of $\kappa_{ele} = L\sigma T$, and the Lorenz number L is calculated through a direct carrier-concentration-dependent restructured SPB model [32].

Fig. 1f displays the change in the zT value of the $MgAg_{0.97}Sb_{0.99}$ sample after annealing for two days at 548 K, compared to the as-sintered sample and 523 K annealed sample. Due to the deterioration of both PF and κ_{tot}, the zT value decreases by about 20%. Vacuum annealing at 548 K for two days significantly worsens the microstructure and TE properties. It is obvious that the formation of the impurity phase greatly damages the nanostructure and thus affects the TE properties, as the nanostructure is highly sensitive to temperature. Herein, the poor thermal stability of nanostructured $MgAg_{0.97}Sb_{0.99}$ at 548 K may severely restrict its long-term service stability at higher operating temperatures, and special attention should be paid to temperature control during applications.

Previous experiments yet showed that vacuum-annealing at 548 K for just two days would produce a series of adverse effects while the sample would be stable at 523 K. Therefore, we extended the annealing time to 7, 14, and 28 days to examine its long-term thermal stability at 523 K. XRD patterns of $MgAg_{0.97}Sb_{0.99}$ samples annealed at 523 K for different days show no obvious impurity phase (Fig. S2). All the diffraction peaks can be indexed to the α-MgAgSb phase. The distribution of the second phase cannot be observed in the BSE images of the polished surface (Fig. S3) with the extension of vacuum-annealing time. The point-scanning data obtained by the EPMA with WDS are listed in Table S2, as the atomic percentages of Mg, Ag, and Sb are almost unchanged. The grain size of annealed samples is examined from the observation of fracture morphology by the SEM images (Fig. S4), indicating that long-term annealing at 523 K only affected the grain size slightly. To further examine the grain size and distribution of samples, more than 100 grains were selected for statistics, and the average grain size increases from about 118 nm to 131 nm after annealing for 28 days. The above characterizations demonstrate that nanostructured $MgAg_{0.97}Sb_{0.99}$ has excellent long-term thermal stability at 523 K.

APT measurements were conducted to reveal the correlation details between the microstructure and thermal stability mechanism of nanostructured $MgAg_{0.97}Sb_{0.99}$ samples, especially the GB characteristics and the local composition near or at GBs. Fig. 2 shows the results of APT analysis for the unannealed $MgAg_{0.97}Sb_{0.99}$ sample. The reconstructed APT volume is shown in Fig. 2a, where Mg, Ag and Sb atoms are depicted by purple, grey and blue dots, respectively. Three-dimensional (3D) reconstruction of the distribution of constituent elemental atoms highlights GBs due to segregation. As indicated by the black arrow, the top view of the region denoted by the black box was selected to obtain the 2D-composition maps of Mg, Ag, and Sb atoms, as shown in Fig. 2b, c, d.

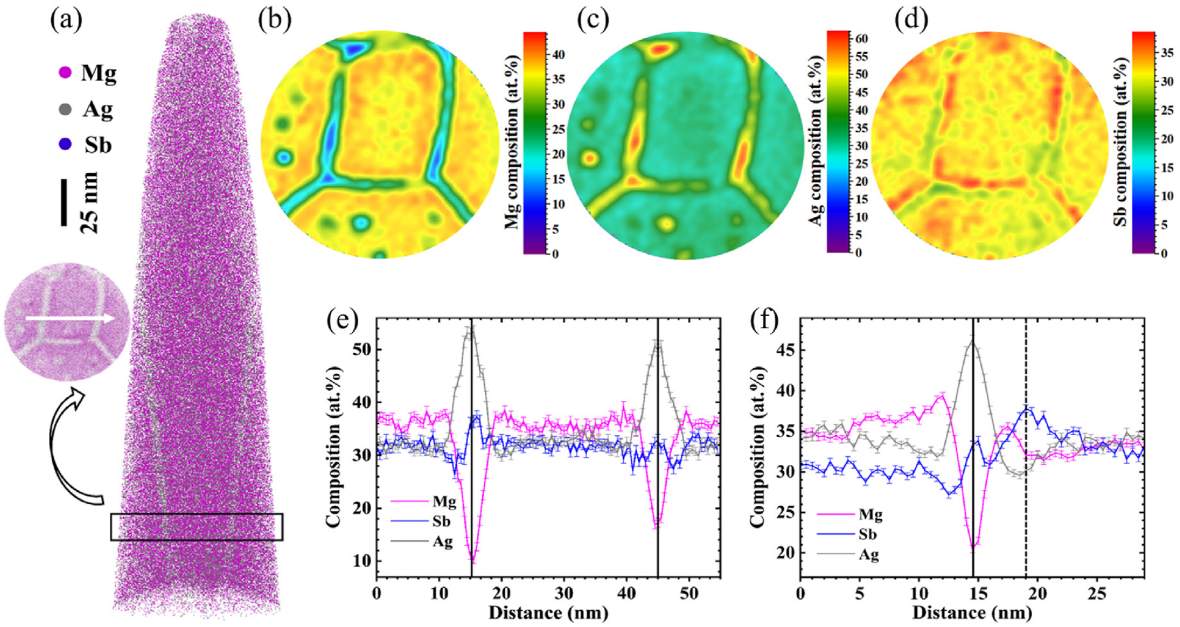

Fig. 2. APT analysis of $MgAg_{0.97}Sb_{0.99}$. (a) 3D reconstruction of the microtip for unannealed sample showing the distribution of Mg, Ag, and Sb atoms by dots of different colors, with the top view of the region marked by the black box, (b–d) 2D-composition map of Mg, Ag, and Sb atoms detected from the top view, (e) 1D-composition profile of unannealed sample across two GBs, as indicated by the white arrow in a, (f) 1D-composition profile of sample annealed for 28 days at 523 K across the GB, as shown by the white arrow in Fig. S5a.

These maps use different color bars to display the degree of Ag and Sb segregation at GBs, with the depletion of Mg. The peaks of the 1D-composition profile (Fig. 2e) across two-grain boundaries give the specific values of Ag atoms segregated at GBs.

The APT results about the $MgAg_{0.97}Sb_{0.99}$ sample annealed at 523 K for 28 days are shown in Fig. S5. After long-term annealing, there is still clearly visible elemental segregation at GBs (Fig. S5a), which is similar to the GB characteristics of unannealed sample. Fig. S5b is the top view of the region denoted by the black box in reconstructed APT volume, as a profile for the generation of 2D-composition maps. From the 2D-composition maps of Mg, Ag, and Sb atoms, it can be seen that the segregation of Ag decreases slightly, as indicated by the value of the color bar (Figs. S5c, d, e). They show no significant changes in elemental distribution near or at GBs, only causing composition homogenization to a certain extent.

It is obvious that grain boundaries exhibit phase-like behavior with the structure and the composition distinctly different from those of the bulk phase due to the segregation of Ag for nanostructured samples, which can be treated as thermodynamically stable equilibrium interfacial states, and the term "complexion" is therefore introduced [33]. GB-associated features of the GB complexions can be discussed more deeply by regarding the composition profile as a function of the distance from the grain interior to the GB core. As shown in Fig. 2e, the composition curve of Ag is accompanied by two adjacent depleted regions near GB-core for the unannealed sample, which can be regarded as GB-segregation with two adjacent depletion zones. This behavior may be due to the formation of the vacancy-solute complex, analogously to the formation of the depleted region in Al-Zn-Mg-Cu alloy [34].

Fig. 2f shows the 1D-composition profile of the area across the grain boundary marked by the white arrow in Fig. S5a. Compared to the results of the unannealed sample, the peak value of Ag concentration decreases from about 54% to 46%. Moreover, the composition profile of the annealed sample can be considered as a moving GB interacts with the segregated solutes. It is obvious that Ag atoms are enriched at GB while Sb atoms are piled up ahead of GB. This result is due to the interaction between grain growth and segregated solutes [35]. For the composition profile in Fig. 2f, the GB migrates from the solid line toward the dotted line position. The resultant broken symmetry of the concentration profile and the GB position brings about a net attractive force between them, which is called the solute drag effect [36]. The driving force for grain coarsening can be suppressed by the solute drag effect on GB migration [37], which can contribute to the kinetic stabilization.

Within the framework of the Gibbs adsorption isotherm, specifically referring to the reduction of GB energy through solute segregation, the concept of thermodynamic stabilization has been proposed and demonstrated as a highly effective approach for stabilizing nanocrystalline materials [38]. The above GB-associated details obtained from 3D APT may be related to the mechanism of thermodynamic stabilization of nanostructured $MgAg_{0.97}Sb_{0.99}$. Regarding the Gibbs adsorption isotherm for the interface, the solute distribution in the bulk and GBs is assumed to follow the Langmuir-McLean segregation equation [39], thus the relation between the GB energy γ and the bulk solute concentration X can be simplified to

$$\gamma = \gamma_0 - \Gamma\left(\Delta H_{seg} + R_g T \ln X\right), \tag{1}$$

where γ_0 is the interfacial energy without segregation, ΔH_{seg} is the enthalpy of segregation, Γ is the Gibbsian interfacial excess of solute at interfaces. To simplify the analysis of stability mechanism, we can obtain the Gibbsian interfacial excess of Ag (Γ_{Ag}) from APT data using the method described by Seidman et al. [40], remaining true to the classical approaches to the thermodynamics of interfaces and suitable for arbitrary geometry [41]. It can be calculated according to the formula $\Gamma_{Ag} = N_{excess}/(\eta_d A)$, where N_{excess} is the total number of atoms in excess at the interface, A is the interfacial area of the selected analysis region, and η_d represents the APT detection efficiency with the value of 50%. Considering that the effectiveness of thermodynamic stabilization depends largely on the magnitude of the reduction in GB energy caused by solute segregation, the calculation of specific interfacial energy value is unnecessary. The ΔH_{seg} should be obtained by complex density functional theory calculations or empirical equation [42], since it is a fixed value for certain elements in the same alloy matrix, we only need to examine the degree of Γ_{Ag} to evaluate the change in GB energy.

For the calculation of Γ_{Ag}, since the detection efficiency and the interfacial area of the selected region are certain values, N_{excess} can be obtained from the ladder diagram of the cumulative number of Ag atoms as a function of the cumulative number of all atoms, as shown in Fig. S6.

The Gibbsian interfacial excess of Ag for the unannealed sample is 7.17 at nm^{-2}, which shows that Ag has a strong segregation tendency at the GB. After annealing for 28 days, remaining a high value of 9.37 at nm^{-2}, the results of average grain size and calculated Γ_{Ag} values are plotted in Table 1. The high degree of Γ_{Ag} before and after annealing at 523 K indicates that the segregation of Ag at GBs led to the reduction of GB energy which can impede the driving force for grain coarsening, contributing to thermodynamic stabilization of nanostructure. Meanwhile, the thermal failure of nanostructure at 548 K can be understood as the transition from GB complexions to GB precipitation makes the grains grow at elevated temperatures [43]. When the temperature is high enough to activate the precipitation of Ag_3Sb, Ag atoms no longer lower the GB free energy by occupying GB sites but form precipitates, resulting in a significant deterioration of thermodynamic stabilization. A comparable phenomenon has been noted in nanocrystalline Ni-P alloys, as the grain size increases due to the formation of the equilibrium Ni_3P phase [44].

The possible explanations for Ag segregation at grain boundaries are inferred as follows. First, Ag presents an abnormal occupied site in the crystal structure, half of the Mg-Sb tetrahedrons are filled by Ag atoms, which is considered to be an unstable filled structure [45,46]. This particular behavior of Ag atoms leads to the weak chemical bonding of Ag-Sb. Secondly, the calculated low defect formation energy of Ag vacancies also indicated the existence of weak Ag bonding [19]. In addition, Mi et al. have found that the atomic displacement parameters (ADPs) of the Ag1 atoms at the 4*a* position are much larger than Ag2 and Ag3, which suggests that there may be a strong static or dynamic disorder of Ag atoms [47]. Experimentally, the positive Γ_{Ag} value in α-MgAgSb indicates that the GB energy can be lowered due to the formation of Ag-rich GB complexions from Gibbs adsorption, similar to the effect in MgB_2-doped $Bi_{0.5}Sb_{1.5}Te_3$ alloys [48].

Changes in TE properties of $MgAg_{0.97}Sb_{0.99}$ samples annealed at 523 K for different days are presented in Fig. 3. With the extension of vacuum annealing time, the ρ at 300 K decreases from 3.56×10^{-5} Ω m to 2.53×10^{-5} Ω m after 28 days (Fig. 3a), and it follows a $T^{1.5}$ dependence before the intrinsic excitation, indicating that the carrier transport is dominated by the acoustic phonon scattering. Fig. 3b shows the room-temperature carrier concentration (n_H) and Hall mobility (μ_H) dependence of annealing days at 523 K. The Hall mobility enhances from 64.86 cm^2 V^{-1} s^{-1} to 76.91 cm^2 V^{-1} s^{-1}, with the carrier concentration varying from 2.7×10^{19} cm^{-3} to 3.3×10^{19} cm^{-3}. Both n_H and μ_H increase with the annealing time, corresponding to the decrease in electrical resistivity as the relationship of $1/\rho = n_H e \mu_H$.

It is noteworthy that the variation of μ_H with n_H due to vacuum annealing (Fig. S7a) is different from the results measured by Liu et al. [16]. Ag vacancy is the dominant intrinsic point defect of α-MgAgSb, which affects the carrier and phonon transport behavior as a donor. It is acknowledged that annealing at the proper temperature can eliminate defects in semiconductors and reduce the vacancy concentration. We suppose that the difference in nanostructured $MgAg_{0.97}Sb_{0.99}$ is due to the influence on the GB composition caused by vacuum annealing at 523 K. For instance in n-type Mg_3Sb_2, Mg deficiency in the GB regions leads to the depletion of free electrons and the formation potential barrier for conduction at the GB, as Mg vacancies are the lowest energy electron killer defects [49]. Correspondingly, the formation of Ag vacancy in p-type α-MgAgSb is accompanied by the appearance of a hole. After annealing for 28 days, it is inferred that the decrease of the peak value of Ag concertation could be related to the increase of Ag vacancies, which may lead to increase of the local n_H near or at GBs, together with the increase of μ_H caused by homogenization at the nanoscale.

Table 1
The average grain size and Gibbsian interfacial excess value of Ag for samples.

Sample	Average grain size (nm)	Γ_{Ag} (at nm^{-2})
As-sintered	118	7.17
28-day annealing at 523 K	131	9.37

Fig. 3c shows the temperature-dependent S varied from annealing time at 523 K, following the same trend with the ρ due to the increased n_H. Values of the carrier concentration dependent S at room temperature all fall nearly on the calculated Pisarenko plots with $m^* = 2.4\ m_0$ (Fig. S7b), similar to the results of Li doping and tuning of Sb content. The calculated power factor PF is presented in Fig. S8a, in which the average power factor $(PF)_{ave}$ was increased from 19.7 μW cm^{-1} K^{-2} to 22.0 μW cm^{-1} K^{-2}. The total thermal conductivity κ_{tot} increases slightly as shown in Fig. 3d. Since the enhancement of power factor is more significant than the change in total thermal conductivity, the zT value at 300 K increases from 1.06 to 1.13, and the average zT value in the entire temperature range increases from 0.7 to 0.79, demonstrating excellent thermal stability of TE properties at 523 K for nanostructured $MgAg_{0.97}Sb_{0.99}$.

Previous investigations on nanostructured $MgAg_{0.97}Sb_{0.99}$ before and after annealing have revealed that the long-term thermal stability at 523 K is satisfactory. However, both microstructure and TE properties are sensitive to the increase of annealing temperature, which is necessary to take relevant strategies to avoid. Grain boundary segregation engineering (GBSE) is always introduced to metallic alloys as a pathway to the design of interfaces, which is applied to ceramic materials and semiconductors. Alloying elements are usually added to pure nanostructured materials as microstructural stabilizers to prevent grain growth through kinetic and thermodynamic mechanisms [50]. The strategy of GBSE has been studied in property optimization of oxide ceramics TE materials, such as tuning the dopant segregation to control GB nanostructures [51,52] or GB phase segregation [53]. Just recently, it was reported that the segregation of Ag dopant at the CdTe/SnTe interface suppressed the Ostwald ripening of nanoprecipitates by lowering the interfacial energy [54].

Therefore, we experimentally investigate the possible role of GBSE in the thermal stability of nanostructured α-MgAgSb. A small amount of Cu substitution for $MgAg_{0.97}Sb_{0.99}$ not only decreases the thermal conductivity but also enhances the power factor, leading to increasing zT values. Sui et al. reported that the solubility limit of Cu in the $MgAg_{0.97}Sb_{0.99}$ alloy is approximately 0.7% [55]. In order to achieve strong GB segregation of Cu atoms in nanostructured MgAgSb, in this work we first attempted to increase the amount of Cu doping to 10% with the nominal composition of $MgCu_{0.1}Ag_{0.87}Sb_{0.99}$, and the as-sintered sample was then vacuum annealed for 14 days at 548 K.

XRD patterns of $MgCu_{0.1}Ag_{0.87}Sb_{0.99}$ samples before and after vacuum annealing at 548 K are shown in Fig. S9. All the diffraction peaks can be well fitted by the α-MgAgSb phase and the MgCuSb phase, indicating that excessive Cu doping leads to a composite of the MgCuSb second phase and the matrix phase. After annealing for 14 days at 548 K, no noticeable impurity phases can be observed in the XRD pattern. The BSE images (Figs. S10a and b) show no significant impurity phase distribution after annealing, there appear only the matrix phase and MgCuSb phase in addition to a few nanopores. The elemental distributions determined by energy dispersive X-ray spectroscopy (EDS) confirm the existence of the MgCuSb phase, as displayed in Fig. S11. From the fracture morphology shown in Figs. S10c and d, the grains are densely arranged without abnormal grain growth. The average grain size increases from about 115 nm to 140 nm after annealing, without abnormal grain growth.

We conducted APT characterizations on the as-sintered $MgCu_{0.1}Ag_{0.87}Sb_{0.99}$ sample to investigate GB-associated features. In the 3D APT reconstruction volume shown in Fig. 4a, Ag atoms and Cu atoms are depicted in grey and orange, respectively. The Ag isocomposition surfaces highlight the segregation of Ag atoms at GBs. As an illustration for the figure, the top view of the region denoted by the box in the microtip contains a triple junction of GBs, where a Cu-rich precipitate can also be identified on the upper left region with a much higher point cloud density of Cu atoms. The segregation of Ag atoms also occurs at the boundary of Cu-rich precipitate, which is the MgCuSb/MgAgSb phase boundary (PB). From the spatial distribution of Ag atoms displayed in Fig. S12, we can observe the presence of three grains. Fig. 4d plots the 1D-composition profile across the GB region denoted by the

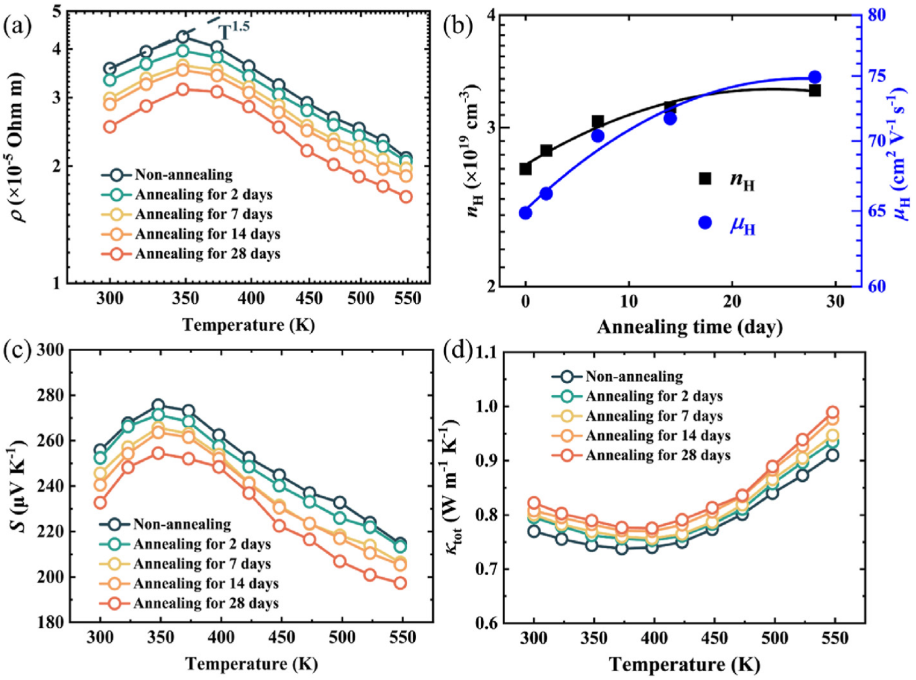

Fig. 3. Temperature-dependent TE properties of $MgAg_{0.97}Sb_{0.99}$ samples annealed at 523 K for different days: (a) electrical resistivity ρ, (b) Hall carrier concentration n_H and Hall carrier mobility μ_H at room temperature, (c) Seebeck coefficient S, (d) total thermal conductivity κ_{tot}.

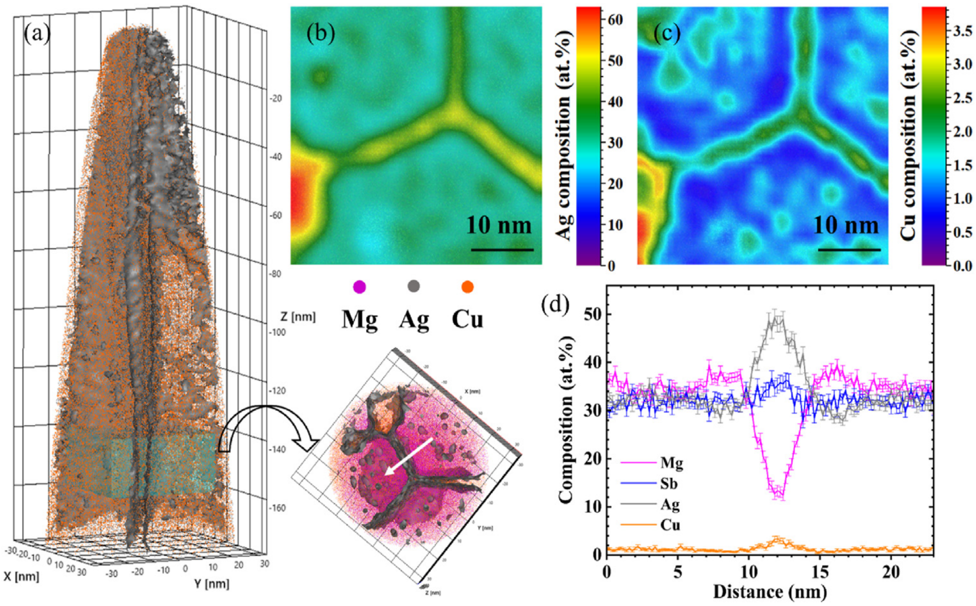

Fig. 4. APT analysis of the as-sintered $MgCu_{0.1}Ag_{0.87}Sb_{0.99}$ sample: (a) 3D reconstruction of the microtip, where Cu atoms are depicted by orange and Ag iso-composition surfaces are depicted by grey, top view of the region denoted by the box displays spatial distribution of constituent element atoms, (b, c) 2D-composition map of Cu and Ag atoms detected from the top view in a, (d) 1D-composition profile across the grain boundary as indicated by the white arrow in a.

white arrow, the layer of about 10 nm width rich in Ag and Cu atoms shows that excessive Cu doping leads to the GB segregation of alloy elements, as is expected. In addition, we found another microtip containing the MgCuSb phase (Fig. S13a). The spatial distribution of Ag atoms (Fig. S13b) shows the presence of Ag-rich GB network and MgCuSb phase. From the 1D-composition profile across the phase boundary, it is obviously seen that Ag atoms also segregate at the PBs.

For the as-sintered $MgCu_{0.1}Ag_{0.87}Sb_{0.99}$ sample, we also obtained Γ_{Ag} and Γ_{Cu} from the ladder diagram of the cumulative number of Ag atoms or Cu atoms as a function of all atoms. As shown in Fig. S14, the calculated Γ_{Ag} is 7.76 at nm^{-2} and Γ_{Cu} is 0.58 at nm^{-2}. We found that the segregation of Ag atoms at GBs is still maintained at the expected degree after excessive Cu doping, even higher than the unannealed $MgAg_{0.97}Sb_{0.99}$ sample (7.17 at nm^{-2}). Moreover, Cu atoms segregating at GBs will further reduce the interfacial energy as an addition to Eq. (1), which can be regarded as a suitable alloying element for stabilizing the microstructure. Therefore, Cu and Ag atoms indicate a tendency of co-segregation at GBs and increase the reduction of GB energy, ensuring better thermodynamic stabilization than $MgAg_{0.97}Sb_{0.99}$. In addition, Cu atoms exhibit a strong GB segregation tendency, not only the reduction of

GB energy can be achieved, but also the solute drag effect may be significant if Cu atoms have a low diffusivity in the matrix, where kinetic stabilization can contribute to the enhanced stability due to the reduction of GB mobility caused by extra drag force of Cu.

Fig. 5 displays the temperature-dependent TE properties of the $MgCu_{0.1}Ag_{0.87}Sb_{0.99}$ sample annealed for 14 days at 548 K in contrast to the as-sintered sample. The electrical resistivity at 300 K decreases from 2.12×10^{-5} Ω m in the as-sintered sample to 1.79×10^{-5} Ω m after the vacuum-annealing process, as shown in Fig. 5a. Change in Seebeck coefficient is shown in Fig. 5b. Since the S only slightly reduces, it can be inferred that the carrier concentration n_H has not changed significantly. Therefore, the decrease in ρ can be attributed to the increase in carrier mobility μ_H, which is derived from homogenization at the nanoscale. The calculated power factor is plotted in Fig. 5c, the room-temperature PF increases from 21.5 $\mu W\ cm^{-1}\ K^{-2}$ to 24.2 $\mu W\ cm^{-1}\ K^{-2}$ in the entire temperature range, due to the reduction of ρ and no significant change in S. The electrical properties of our sample were doubly checked by a laboratory in Russia to verify the reliability of our measurements, the properties are quite comparable, as shown in Fig. S15.

The calculation results of the total thermal conductivity of $MgCu_{0.1}Ag_{0.87}Sb_{0.99}$ sample annealed at 548 K for 14 days are shown in Fig. 5d. Compared with the unannealed sample, the room-temperature κ_{tot} increases from 0.95 $W\ m^{-1}\ K^{-1}$ to 1.06 $W\ m^{-1}\ K^{-1}$, without sharp deterioration. Since the calculated L only slightly changes, the increase of electronic thermal conductivity κ_{ele} can be ascribed to the decrease of ρ. For the lattice thermal conductivity κ_{lat}, the room-temperature value shows no obvious change, only increases from 0.72 $W\ m^{-1}\ K^{-1}$ to 0.80 $W\ m^{-1}\ K^{-1}$, as shown in Fig. 5e. It can be interpreted that the increase in κ_{lat} may be due to the decrease of Ag vacancy concentration caused by annealing at 548 K, which weakens the strong phonon scattering by vacancies.

Fig. 5f shows the zT value of the $MgCu_{0.1}Ag_{0.87}Sb_{0.99}$ sample after annealing. Although the total thermal conductivity increases, the improved power factor compensates for its change to some extent. The zT changes within 10% compared to the unannealed sample. There is no significant damage to the microstructure, and TE properties after 14 days of annealing with the high room-temperature zT of around 0.7 indicate that the nanostructured $MgCu_{0.1}Ag_{0.87}Sb_{0.99}$ demonstrates better thermal stability at 548 K than the pure $MgAg_{0.97}Sb_{0.99}$ sample, related to the GB segregation of extra Cu atoms.

4. Conclusion

In summary, we have characterized the microstructure and evaluated thermoelectric properties of p-type nanostructured α-MgAgSb before and after vacuum annealing. APT measurements were conducted to reveal details of grain boundary complexions to explain the mechanism of thermal stability. Annealing at 548 K for two days causes abnormal grain growth and reduces TE properties due to the formation of impurity phase. Under 523 K, the segregation of Ag at GBs can achieve the reduction of GB energy and solute drag effect, ensuring excellent long-term thermodynamic and kinetic stabilization. According to the concept of GBSE, excessive Cu doping realizes additional GB segregation without reducing the segregation of Ag at GBs and PBs, making the final compound thermally stable after annealing at 548 K for 14 days with the room-temperature zT of around 0.7. Our results show that the selection of suitable doping elements can stabilize the nanostructure through GB segregation. This, in turn, contributes to designs of highly stable and high-performance nanostructured bulk thermoelectric materials.

CRediT authorship contribution statement

Lei Jiao: Writing – original draft, Methodology, Investigation, Data curation, Conceptualization. **Liangjun Xie:** Validation, Investigation, Data curation, Conceptualization. **Yu-Ke Zhu:** Resources, Methodology, Investigation. **Lankun Wang:** Methodology, Investigation. **Yuxin Sun:** Methodology, Investigation. **Yuan Yu:** Writing – review & editing, Visualization, Supervision, Methodology, Data curation. **Alexandra Ivanova:** Validation, Methodology, Data curation. **Vladimir Khovaylo:** Writing – review & editing, Validation, Supervision. **Fengkai Guo:** Supervision, Project administration. **Wei Cai:** Supervision, Project administration. **Jiehe Sui:** Writing – review & editing, Supervision, Resources,

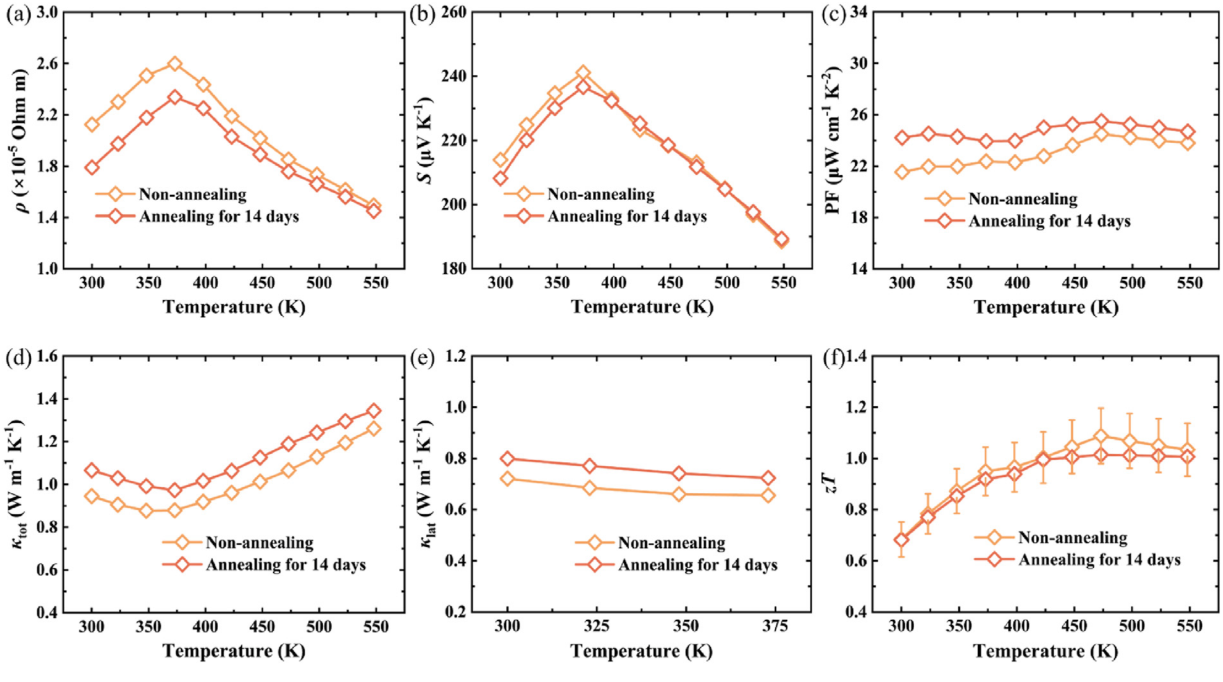

Fig. 5. Temperature-dependent TE properties of $MgCu_{0.1}Ag_{0.87}Sb_{0.99}$ annealed for 14 days at 548 K. (a) Electrical resistivity ρ, (b) Seebeck coefficient S, (c) power factor (PF), (d) total thermal conductivity κ_{tot}, (e) lattice thermal conductivity κ_{lat}, (f) figure of merit zT.

Funding acquisition. **Zihang Liu:** Writing – review & editing, Supervision, Methodology, Funding acquisition, Conceptualization.

Declaration of competing interest

The authors declare that they have no known competing financial interests or personal relationships that could have appeared to influence the work reported in this paper.

Acknowledgements

This work was supported by the National Natural Science Foundation of China (22409043, 52130106 and 523B2020), the Natural Science Foundation of Heilongjiang Province (LH2023E032), and the State Key Laboratory for Mechanical Behavior of Materials (20232507).

Appendix A. Supplementary data

Supplementary data to this article can be found online at https://doi.org/10.1016/j.tramat.2025.100016.

References

[1] Z. Bu, X. Zhang, Y. Hu, Z. Chen, S. Lin, W. Li, C. Xiao, Y. Pei, A record thermoelectric efficiency in tellurium-free modules for low-grade waste heat recovery, Nat. Commun. 13 (2022) 237, https://doi.org/10.1038/s41467-021-27916-y.

[2] X.-L. Shi, J. Zou, Z.-G. Chen, Advanced thermoelectric design: from materials and structures to devices, Chem. Rev. 120 (2020) 7399–7515, https://doi.org/10.1021/acs.chemrev.0c00026.

[3] W. Liu, Q. Jie, H. Kim, Z. Ren, Current progress and future challenges in thermoelectric power generation: from materials to devices, Acta Mater. 87 (2015) 357–376, https://doi.org/10.1016/j.actamat.2014.12.042.

[4] G.J. Snyder, E.S. Toberer, Complex thermoelectric materials, Nat. Mater. 7 (2008) 105–114, https://doi.org/10.1038/nmat2090.

[5] J. Mao, Z. Liu, J. Zhou, H. Zhu, Q. Zhang, G. Chen, Z. Ren, Advances in thermoelectrics, Adv. Phys. 67 (2018) 69–147, https://doi.org/10.1080/00018732.2018.1551715.

[6] G. Tan, L.-D. Zhao, M.G. Kanatzidis, Rationally designing high-performance bulk thermoelectric materials, Chem. Rev. 116 (2016) 12123–12149, https://doi.org/10.1021/acs.chemrev.6b00255.

[7] F. Hao, P. Qiu, Y. Tang, S. Bai, T. Xing, H.-S. Chu, Q. Zhang, P. Lu, T. Zhang, D. Ren, J. Chen, X. Shi, L. Chen, High efficiency Bi_2Te_3-based materials and devices for thermoelectric power generation between 100 and 300 degrees °C, Energy Environ. Sci. 9 (2016) 3120–3127, https://doi.org/10.1039/c6ee02017h.

[8] Z. Zhou, G. Han, X. Lu, G. Wang, X. Zhou, High-performance magnesium-based thermoelectric materials: progress and challenges, J. Magnesium Alloys 10 (2022) 1719–1736, https://doi.org/10.1016/j.jma.2022.05.021.

[9] X. Zhang, N. Chen, K. Guo, Q. Zhang, Q. Zhao, J. Xu, H. Zhu, H. Zhao, High cooling and power generation performance of α-MgAgSb with intrinsic low lattice thermal conductivity, Mater. Today Phys. 44 (2024) 101451, https://doi.org/10.1016/j.mtphys.2024.101451.

[10] Z. Liu, W. Gao, X. Meng, X. Li, J. Mao, Y. Wang, J. Shuai, W. Cai, Z. Ren, J. Sui, Mechanical properties of nanostructured thermoelectric materials α-MgAgSb, Scr. Mater. 127 (2017) 72–75, https://doi.org/10.1016/j.scriptamat.2016.08.037.

[11] Y. Huang, J. Lei, H. Chen, Z. Zhou, H. Dong, S. Yang, H. Gao, T.-R. Wei, K. Zhao, X. Shi, Intrinsically high thermoelectric performance in near-room-temperature α-MgAgSb materials, Acta Mater. 249 (2023) 118847, https://doi.org/10.1016/j.actamat.2023.118847.

[12] D. Kraemer, J. Sui, K. McEnaney, H. Zhao, Q. Jie, Z.F. Ren, G. Chen, High thermoelectric conversion efficiency of MgAgSb-based material with hot-pressed contacts, Energy Environ. Sci. 8 (2015) 1299–1308, https://doi.org/10.1039/c4ee02813a.

[13] M.J. Kirkham, A.M. dos Santos, C.J. Rawn, E. Lara-Curzio, J.W. Sharp, A.J. Thompson, Abinitio determination of crystal structures of the thermoelectric material MgAgSb, Phys. Rev. B 85 (2012) 114120, https://doi.org/10.1103/PhysRevB.85.144120.

[14] H. Zhao, J. Sui, Z. Tang, Y. Lan, Q. Jie, D. Kraemer, K. McEnaney, A. Guloy, G. Chen, Z. Ren, High thermoelectric performance of MgAgSb-based materials, Nano Energy 7 (2014) 97–103, https://doi.org/10.1016/j.nanoen.2014.04.012.

[15] P. Ying, X. Liu, C. Fu, X. Yue, H. Xie, X. Zhao, W. Zhang, T. Zhu, High performance α-MgAgSb thermoelectric materials for low temperature power generation, Chem. Mater. 27 (2015) 909–913, https://doi.org/10.1021/cm5041826.

[16] Z. Liu, Y. Wang, J. Mao, H. Geng, J. Shuai, Y. Wang, R. He, W. Cai, J. Sui, Z. Ren, Lithium doping to enhance thermoelectric performance of MgAgSb with weak electron-phonon coupling, Adv. Energy Mater. 6 (2016) 1502269, https://doi.org/10.1002/aenm.201502269.

[17] Z. Liu, J. Shuai, J. Mao, Y. Wang, Z. Wang, W. Cai, J. Sui, Z. Ren, Effects of antimony content in $MgAg_{0.97}Sb_x$ on output power and energy conversion efficiency, Acta Mater. 102 (2016) 17–23, https://doi.org/10.1016/j.actamat.2015.09.033.

[18] Z. Liu, Y. Zhang, J. Mao, W. Gao, Y. Wang, J. Shuai, W. Cai, J. Sui, Z. Ren, The microscopic origin of low thermal conductivity for enhanced thermoelectric performance of Yb doped MgAgSb, Acta Mater. 128 (2017) 227–234, https://doi.org/10.1016/j.actamat.2017.02.015.

[19] Z. Liu, H. Geng, J. Mao, J. Shuai, R. He, C. Wang, W. Cai, J. Sui, Z. Ren, Understanding and manipulating the intrinsic point defect in α-MgAgSb for higher thermoelectric performance, J. Mater. Chem. A 4 (2016) 16834–16840, https://doi.org/10.1039/c6ta06832d.

[20] P. Ying, R. He, J. Mao, Q. Zhang, H. Reith, J. Sui, Z. Ren, K. Nielsch, G. Schierning, Towards tellurium-free thermoelectric modules for power generation from low-grade heat, Nat. Commun. 12 (2021) 1121, https://doi.org/10.1038/s41467-021-21391-1.

[21] Z. Liu, N. Sato, W. Gao, K. Yubuta, N. Kawamoto, M. Mitome, K. Kurashima, Y. Owada, K. Nagase, C.-H. Lee, J. Yi, K. Tsuchiya, T. Mori, Demonstration of ultrahigh thermoelectric efficiency of ~7.3% in Mg_3Sb_2/MgAgSb module for low-temperature energy harvesting, Joule 5 (2021) 1196–1208, https://doi.org/10.1016/j.joule.2021.03.017.

[22] P. Ying, L. Wilkens, H. Reith, N.P. Rodriguez, X. Hong, Q. Lu, C. Hess, K. Nielsch, R. He, A robust thermoelectric module based on MgAgSb/$Mg_3(Sb,Bi)_2$ with a conversion efficiency of 8.5% and a maximum cooling of 72 K, Energy Environ. Sci. 15 (2022) 2557–2566, https://doi.org/10.1039/d2ee00883a.

[23] X. Wu, Y. Lin, C. Liu, Y. Wang, H. Li, B. Ge, W. Liu, A high performance eco-friendly MgAgSb-based thermoelectric power generation device near phase transition temperatures, Energy Environ. Sci. 17 (2024) 2879–2887, https://doi.org/10.1039/d4ee00019f.

[24] N. Liang, Y. Zhao, A review on thermal stability of nanostructured materials, J. Alloys Compd. 938 (2023) 168528, https://doi.org/10.1016/j.jallcom.2022.168528.

[25] K. Lu, Stabilizing nanostructures in metals using grain and twin boundary architectures, Nat. Rev. Mater. 1 (2016) 16019, https://doi.org/10.1038/natrevmats.2016.19.

[26] H.R. Peng, M.M. Gong, Y.Z. Chen, F. Liu, Thermal stability of nanocrystalline materials: thermodynamics and kinetics, Int. Mater. Rev. 62 (2017) 303–333, https://doi.org/10.1080/09506608.2016.1257536.

[27] H. Qin, J. Zhu, N. Li, H. Wu, F. Guo, S. Sun, D. Qin, S.J. Pennycook, Q. Zhang, W. Cai, J. Sui, Enhanced mechanical and thermoelectric properties enabled by hierarchical structure in medium-temperature Sb2Te3 based alloys, Nano Energy 78 (2020) 105228, https://doi.org/10.1016/j.nanoen.2020.105228.

[28] S.A. Yamini, M. Brewis, J. Byrnes, R. Santos, A. Manettas, Y.Z. Pei, Fabrication of thermoelectric materials – thermal stability and repeatability of achieved efficiencies, J. Mater. Chem. C 3 (2015) 10610–10615, https://doi.org/10.1039/c5tc02210j.

[29] B. Poudel, Q. Hao, Y. Ma, Y. Lan, A. Minnich, B. Yu, X. Yan, D. Wang, A. Muto, D. Vashaee, X. Chen, J. Liu, M.S. Dresselhaus, G. Chen, Z. Ren, High-thermoelectric performance of nanostructured bismuth antimony telluride bulk alloys, Science 320 (2008) 634–638, https://doi.org/10.1126/science.1156446.

[30] K. Biswas, J. He, I.D. Blum, C.-I. Wu, T.P. Hogan, D.N. Seidman, V.P. Dravid, M.G. Kanatzidis, High-performance bulk thermoelectrics with all-scale hierarchical architectures, Nature 489 (2012) 414–418, https://doi.org/10.1038/nature11439.

[31] L. Xie, J. Yang, Z. Liu, N. Qu, X. Dong, J. Zhu, W. Shi, H. Wu, G. Peng, F. Guo, Y. Zhang, W. Cai, H. Wu, H. Zhu, H. Zhao, Z. Liu, J. Sui, Highly efficient thermoelectric cooling performance of ultrafine-grained and nanoporous materials, Mater. Today 65 (2023) 5–13, https://doi.org/10.1016/j.mattod.2023.03.021.

[32] J. Zhu, X. Zhang, M. Guo, J. Li, J. Hu, S. Cai, W. Cai, Y. Zhang, J. Sui, Restructured single parabolic band model for quick analysis in thermoelectricity, npj Comput. Mater. 7 (2021) 116, https://doi.org/10.1038/s41524-021-00587-5.

[33] P.R. Cantwell, M. Tang, S.J. Dillon, J. Luo, G.S. Rohrer, M.P. Harmer, Grain boundary complexions, Acta Mater. 62 (2014) 1–48, https://doi.org/10.1016/j.actamat.2013.07.037.

[34] H. Zhao, F. De Geuser, A.K. da Silva, A. Szczepaniak, B. Gault, D. Ponge, D. Raabe, Segregation assisted grain boundary precipitation in a model Al-Zn-Mg-Cu alloy, Acta Mater. 156 (2018) 318–329, https://doi.org/10.1016/j.actamat.2018.07.003.

[35] T. Luo, D. Mangelinck, F. Serrano-Sanchez, C. Fu, C. Felser, B. Gault, Grain boundary in NbCo(Pt)Sn half-Heusler compounds: segregation and solute drag on grain boundary migration, Acta Mater. 226 (2022) 117604, https://doi.org/10.1016/j.actamat.2021.117604.

[36] S.G. Kim, Y.B. Park, Grain boundary segregation, solute drag and abnormal grain growth, Acta Mater. 56 (2008) 3739–3753, https://doi.org/10.1016/j.actamat.2008.04.007.

[37] M. Hillert, Solute drag in grain boundary migration and phase transformations, Acta Mater. 52 (2004) 5289–5293, https://doi.org/10.1016/j.actamat.2004.07.032.

[38] D. Raabe, M. Herbig, S. Sandloebes, Y. Li, D. Tytko, M. Kuzmina, D. Ponge, P.P. Choi, Grain boundary segregation engineering in metallic alloys: a pathway to the design of interfaces, Curr. Opin. Solid State Mater. Sci. 18 (2014) 253–261, https://doi.org/10.1016/j.cossms.2014.06.002.

[39] R. Kirchheim, Grain coarsening inhibited by solute segregation, Acta Mater. 50 (2002) 413–419, https://doi.org/10.1016/s1359-6454(01)00338-x.

[40] B.W. Krakauer, D.N. Seidman, Absolute atomic-scale measurements of the Gibbsian interfacial excess of solute at internal interfaces, Phys. Rev. B 48 (1993) 6724–6727, https://doi.org/10.1103/PhysRevB.48.6724.

[41] O.C. Hellman, D.N. Seidman, Measurement of the Gibbsian interfacial excess of solute at an interface of arbitrary geometry using three-dimensional atom probe microscopy, Mater. Sci. Eng., A 327 (2002) 24–28, https://doi.org/10.1016/s0921-5093(01)01885-8.

[42] P.C. Millett, R.P. Selvam, A. Saxena, Stabilizing nanocrystalline materials with dopants, Acta Mater. 55 (2007) 2329–2336, https://doi.org/10.1016/j.actamat.2006.11.028.

[43] C. Zhang, G. Yan, Y. Wang, X. Wu, L. Hu, F. Liu, W. Ao, O. Cojocaru-Mirédin, M. Wuttig, G.J. Snyder, Y. Yu, Grain boundary complexions enable a simultaneous optimization of electron and phonon transport leading to high-performance GeTe thermoelectric devices, Adv. Energy Mater. 13 (2022) 2203361, https://doi.org/10.1002/aenm.202203361.

[44] B. Färber, E. Cadel, A. Menand, G. Schmitz, R. Kirchheim, Phosphorus segregation in nanocrystalline Ni-3.6 at.% P alloy investigated with the tomographic atom probe (TAP), Acta Mater. 48 (2000) 789–796, https://doi.org/10.1016/s1359-6454(99)00397-3.

[45] D. Li, H. Zhao, S. Li, B. Wei, J. Shuai, C. Shi, X. Xi, P. Sun, S. Meng, L. Gu, Z. Ren, X. Chen, Atomic disorders induced by silver and magnesium ion migrations favor high thermoelectric performance in α-MgAgSb-based materials, Adv. Funct. Mater. 25 (2015) 6478–6488, https://doi.org/10.1002/adfm.201503022.

[46] P. Ying, X. Li, Y. Wang, J. Yang, C. Fu, W. Zhang, X. Zhao, T. Zhu, Hierarchical chemical bonds contributing to the intrinsically low thermal conductivity in alpha-MgAgSb thermoelectric materials, Adv. Funct. Mater. 27 (2017) 1604145, https://doi.org/10.1002/adfm.201604145.

[47] J.-L. Mi, P.-J. Ying, M. Sist, H. Reardon, P. Zhang, T.-J. Zhu, X.-B. Zhao, B.B. Iversen, Elaborating the crystal structures of MgAgSb thermoelectric compound: polymorphs and atomic disorders, Chem. Mater. 29 (2017) 6378–6388, https://doi.org/10.1021/acs.chemmater.7b01768.

[48] C. Zhang, Q. Lai, W. Wang, X. Zhou, K. Lan, L. Hu, B. Cai, M. Wuttig, J. He, F. Liu, Y. Yu, Gibbs adsorption and zener pinning enable mechanically robust high-performance Bi_2Te_3-based thermoelectric devices, Adv. Sci. 10 (2023) 2302688, https://doi.org/10.1002/advs.202302688.

[49] J.J. Kuo, Y. Yu, S.D. Kang, O. Cojocaru-Mirédin, M. Wuttig, G.J. Snyder, Mg deficiency in grain boundaries of n-type Mg_3Sb_2 identified by atom probe tomography, Adv. Mater. Interfac. 6 (2019) 1900429, https://doi.org/10.1002/admi.201900429.

[50] T. Chookajorn, H.A. Murdoch, C.A. Schuh, Design of stable nanocrystalline alloys, Science 337 (2012) 951–954, https://doi.org/10.1126/science.1224737.

[51] C. Boyle, P. Carvillo, Y. Chen, E.J. Barbero, D. McIntyre, X. Song, Grain boundary segregation and thermoelectric performance enhancement of bismuth doped calcium cobaltite, J. Eur. Ceram. Soc. 36 (2016) 601–607, https://doi.org/10.1016/j.jeurceramsoc.2015.10.042.

[52] C. Romo-De-La-Cruz, L. Liang, S.A.P. Navia, Y. Chen, J. Prucz, X. Song, Role of oversized dopant potassium on the nanostructure and thermoelectric performance of calcium cobaltite ceramics, Sustain. Energy Fuels 2 (2018) 876–881, https://doi.org/10.1039/c7se00612h.

[53] X. Song, S.A. Paredes Navia, L. Liang, C. Boyle, C.O. Romo-De-La-Cruz, B. Jackson, A. Hinerman, M. Wilt, J. Prucz, Y. Chen, Grain boundary phase segregation for dramatic improvement of the thermoelectric performance of oxide ceramics, ACS Appl. Mater. Interfaces 10 (2018) 39018–39024, https://doi.org/10.1021/acsami.8b12710.

[54] D. An, J. Wang, J. Zhang, X. Zhai, Z. Kang, W. Fan, J. Yan, Y. Liu, L. Lu, C.-L. Jia, M. Wuttig, O. Cojocaru-Miredin, S. Chen, W. Wang, G.J. Snyder, Y. Yu, Retarding Ostwald ripening through Gibbs adsorption and interfacial complexions leads to high-performance SnTe thermoelectrics, Energy Environ. Sci. 14 (2021) 5469–5479, https://doi.org/10.1039/d1ee01977e.

[55] J. Sui, J. Shuai, Y. Lan, Y. Liu, R. He, D. Wang, Q. Jie, Z. Ren, Effect of Cu concentration on thermoelectric properties of nanostructured p-type $MgAg_{0.97-x}Cu_xSb_{0.99}$, Acta Mater. 87 (2015) 266–272, https://doi.org/10.1016/j.actamat.2015.01.018.